

Simulating the one-dimensional structure of Titan's upper atmosphere:

3. Mechanisms determining methane escape

Jared M. Bell,¹ Stephen W. Bougher,² J. Hunter Waite Jr.,¹ Aaron J. Ridley,² Brian A. Magee,¹ Kathleen E. Mandt,^{1,3} Joseph Westlake,⁴ Anna D. DeJong,¹ Akiva Bar-Nun,⁵ Ronen Jacovi,⁶ Gabor Toth,² Virginie De La Haye,¹ David Gell,¹ and Gregory Fletcher¹

Received 28 April 2010; revised 1 September 2011; accepted 7 September 2011; published 12 November 2011.

[1] This investigation extends the work presented by Bell et al. (2010a, 2010b). Using the one-dimensional (1-D) configuration of the Titan Global Ionosphere-Thermosphere Model (T-GITM), we quantify the relative importance of the different dynamical and chemical mechanisms that determine the CH₄ escape rates calculated by T-GITM. Moreover, we consider the implications of updated Huygens Gas Chromatograph Mass Spectrometer (GCMS) determinations of both the ⁴⁰Ar mixing ratios and ¹⁵N/¹⁴N isotopic ratios in work by Niemann et al. (2010). Combining the GCMS constraints in the lower atmosphere with the Ion Neutral Mass Spectrometer (INMS) measurements in work by Magee et al. (2009), our simulation results suggest that the optimal CH₄ homopause altitude is located at 1000 km. Using this homopause altitude, we conclude that topside escape rates of 1.0×10^{10} CH₄ m⁻² s⁻¹ (referred to the surface) are sufficient to reproduce the INMS methane measurements in work by Magee et al. (2009). These escape rates of methane are consistent with the upper limits to methane escape (1.11×10^{11} CH₄ m⁻² s⁻¹) established by both the Cassini Plasma Spectrometer (CAPS) and Magnetosphere Imaging Instrument (MIMI) measurements of Carbon-group ions in the near Titan magnetosphere.

Citation: Bell, J. M., et al. (2011), Simulating the one-dimensional structure of Titan's upper atmosphere: 3. Mechanisms determining methane escape, *J. Geophys. Res.*, 116, E11002, doi:10.1029/2010JE003639.

1. Introduction

1.1. Scientific Motivation

[2] The works by *Strobel* [2008, 2009, 2010] and *Yelle et al.* [2008] inferred that CH₄ was escaping Titan at rates of up to 44–66 kg/s globally ($\sim 2.0\text{--}3.0 \times 10^{13}$ CH₄ m⁻² s⁻¹), and they have suggested that these high outflows of methane are required to reproduce Ion Neutral Mass Spectrometer (INMS) [*Waite et al.*, 2004] composition. However, Direct Simulation Monte Carlo (DSMC) calculations by *Tucker*

and *Johnson* [2009] indicated that this outflow was neither necessary to reproduce INMS data, nor was it calculated by the DSMC model. Furthermore, recent analysis of the Cassini Plasma Spectrometer (CAPS) Ion Mass Spectrometer (IMS) and the Magnetospheric Imaging Instrument (MIMI) Charge Energy Mass Spectrometer (CHEMS) revealed that Carbon-group ions near Titan's orbit in Saturn's magnetosphere impose an upper limit of $\sim 1.1 \times 10^{11}$ CH₄ m⁻² s⁻¹ (or roughly 0.22 kg s⁻¹, globally) on the neutral carbon outflow from Titan [*Crary et al.*, 2010; *Smith et al.*, 2009].

[3] *Bell et al.* [2010a, 2010b] (hereinafter referred to as part 1 and part 2, respectively) sought to simulate configurations of Titan's upper atmosphere, between 500 km and 1500 km, that could reproduce the average INMS mixing ratios and densities between TA and T40 with high accuracy. Using the Titan Global Ionosphere-Thermosphere Model (T-GITM), the authors presented simulations that self-consistently calculated the upper atmosphere's composition, thermal structure, and vertical dynamics. The major results from these two initial studies were that: (1) the uncertainties in our current knowledge of the temperatures and densities between 500 km and 1000 km allow for a wide range of potential configurations of Titan's upper atmo-

¹Division of Space Science and Engineering, Southwest Research Institute, San Antonio, Texas, USA.

²Department of Atmospheric, Oceanic, and Space Sciences, University of Michigan, Ann Arbor, Michigan, USA.

³Department of Civil and Environmental Engineering, University of Texas at San Antonio, San Antonio, Texas, USA.

⁴Department of Physics and Astronomy, University of Texas at San Antonio, San Antonio, Texas, USA.

⁵Department of Geophysics and Planetary Sciences, Tel Aviv University, Tel Aviv, Israel.

⁶Ice Spectroscopy Laboratory, Jet Propulsion Laboratory, California Institute of Technology, Pasadena, California, USA.

sphere and (2) given these large uncertainties, there exist simulated configurations of Titan's upper atmosphere that can reproduce INMS composition with high accuracy while using low escape rates of methane.

[4] In particular, *Bell et al.* [2010b] demonstrated that T-GITM could reproduce the INMS composition of *Magee et al.* [2009] using CH₄ escape fluxes of $\sim 1.0 \times 10^8$ molecules $\text{m}^{-2} \text{s}^{-1}$, which fell within the upper limits imposed by the CAPS and MIMI magnetosphere carbon ion measurements. The low methane escape scenarios were achieved when using: (1) a methane homopause of roughly 1000 km or (2) a methane homopause of roughly 950 km combined with aerosol trapping as an additional loss process for methane. Moreover, *Bell et al.* [2010b] found that the topside escape rates of CH₄ required to match the INMS methane measurements varied significantly among the ten different configurations presented, suggesting that the T-GITM estimates for methane escape were sensitive to variations in the different simulations' thermal structures, density structures, methane homopause altitudes, and total methane chemical destruction.

[5] Ultimately, in work by *Bell et al.* [2010b], we found that three key variables appeared to impact the model's simulated methane densities and topside escape rates: (1) the lower boundary methane mixing ratios (at 500 km), (2) the total amount of turbulence in the simulation (i.e., the CH₄ homopause altitude), and (3) the amount of methane chemical destruction included in a given simulation. Moreover, these three parameters were found to be interrelated. For instance, by increasing the amount of turbulence in the atmosphere (i.e., increasing the methane homopause), we could impose higher methane mixing ratios at 500 km and still match the INMS data above 1000 km. Similarly, when reducing the chemical destruction of methane to 0.0 in Model 3 (NC) of *Bell et al.* [2010b], we also found that, in order to match INMS data, we had to reduce the methane mixing ratio at 500 km. However, while parts 1 and 2 isolated some of the parameters needed to reproduce the INMS methane data above 1000 km with T-GITM, we did not explore the details of the chemistry and physics in those simulations.

[6] In this investigation, we expand upon the results of *Bell et al.* [2010a, 2010b] by isolating the different chemical and physical mechanisms that impact the vertical methane fluxes in T-GITM. First, we investigate the vertical fluxes from a representative T-GITM simulation taken from *Bell et al.* [2010b], Model 7. We show that (1) the N₂-CH₄ momentum coupling, and (2) the column-integrated chemistry play major roles in determining the vertical methane escape fluxes required by T-GITM to reproduce INMS composition. Second, we incorporate revised constraints on the methane homopause provided by a recent update to the ⁴⁰Ar abundance and ¹⁴N/¹⁵N isotopic ratio measured by the Huygens Gas Chromatograph Mass Spectrometer (GCMS) in work by *Niemann et al.* [2010]. Using these updated composition constraints, we show that the CH₄ homopause is most likely near 1000 km. Similarly, we illustrate that increasing the total photochemical destruction of methane by $\sim 10\%$ allows T-GITM to simultaneously match both the INMS data and the updated GCMS methane mixing ratio measurements. Finally, we test the uniqueness of the T-GITM results using a separate, 1-D hydrostatic diffusion model that approximates

the model of *Yelle et al.* [2008] and provides an independent estimate for the CH₄ escape rates required to match INMS data.

1.2. Overview of T-GITM

[7] Details of the Titan Global Ionosphere-Thermosphere Model (T-GITM) are provided by *Bell et al.* [2010a, 2010b]. This model is a 3-D non-hydrostatic Global Circulation Model (GCM) that solves the time-dependent Navier-Stokes equations between 500 km and 1500 km on a spherical altitude grid. In this study and in parts 1 and 2, T-GITM operates in a 1-D configuration by neglecting the horizontal components of the Navier-Stokes continuity, momentum, and energy equations. The 1-D T-GITM rotates with the planet, allowing the model to capture the diurnal variations at a specific latitude, as is done by *Bell et al.* [2011]. We carry 15 neutral species (N₂, CH₄, ⁴⁰Ar, HCN, H₂, ¹³CH₄, ¹⁵N-¹⁴N, N(⁴S), H, C₂H₄, ³CH₂, ¹CH₂, CH₃, CH, and H₂CN), 5 ion species (N₂⁺, N⁺, HCNH⁺, CH₃⁺, and C₂H₅⁺), and electrons equal to the total ion content to provide charge neutrality. All species are coupled through a reduced ion-neutral chemical scheme that focuses on the formation of HCN [*Bell et al.*, 2010a].

[8] We specify fixed boundary conditions on the densities, winds, and temperatures at the lower boundary (500 km). These boundary conditions do not evolve over the course of the simulation, and we use the most relevant lower atmospheric data available from Cassini instruments to constrain the temperatures and composition at 500 km [see *Bell et al.*, 2010a, 2010b]. The vertical winds at 500 km are assumed to be zero, since no reliable measurements exist.

[9] At the upper boundary, we assume that the gradients of the winds and temperatures vanish. For H₂ and H, we specify the Jeans escape velocities based upon the temperature at the exobase (roughly 1500 km). For the neutral densities, we assume that the second derivative in the density gradient vanishes across the upper boundary for escaping species (i.e., H₂ and H), while the other major species adopt their molecular diffusive scale height at the upper boundary. This approximation is valid for species that are not escaping (i.e., N₂ and CH₄). If we want to simulate enhanced methane escape, then we can impose an enhanced escape speed for CH₄ at 1500 km consistent with *Strobel* [2009] and *Yelle et al.* [2008]. The most critical boundary conditions for the T-GITM simulations of this investigation are presented in Tables 1 and 2.

[10] In addition to the boundary conditions, the parameterization of turbulence represents a key determinant for the simulated vertical methane fluxes. T-GITM characterizes this turbulence according to the following formulation from *Atreya* [1986]:

$$K(r) = K(0) \sqrt{\frac{N(0)}{N(r)}}, \quad K \leq K_{\max}. \quad (1)$$

In this equation, $K(0)$ and $N(0)$ represent the eddy diffusion coefficient and the total neutral density at the model's lower boundary, respectively, while $K(r)$ and $N(r)$ represent the same parameters at a specific radial distance, r . Finally, K_{\max} is the maximum, asymptotic value for $K(r)$ allowed in a given simulation. This formulation approximates the impacts of

Table 1. Summary of Lower Boundary Settings in Models 7–12 (Aero)^a

	Lower Boundary Settings at 500 km					Turbulence Settings	
	Total Density (molecules/m ³)	T (K)	CH ₄ Mixing Ratio	⁴⁰ Ar Mixing Ratio	¹⁴ N/ ¹⁵ N Isotopic Ratio	K ₀ (m ² /s)	K _{max} (m ² /s)
Model 7	7.74 × 10 ¹⁹	180	1.23 × 10 ⁻²	4.15 × 10 ⁻⁵	—	175.0	30,000.0
Model 11	9.61 × 10 ¹⁹	175	1.25 × 10 ⁻²	3.30 × 10 ⁻⁵	167.7	175.0	3000.0
Model 12	9.14 × 10 ¹⁹	175	1.35 × 10 ⁻²	3.30 × 10 ⁻⁵	167.7	175.0	—
Model 12 (NC)	9.14 × 10 ¹⁹	175	1.10 × 10 ⁻²	3.30 × 10 ⁻⁵	167.7	175.0	—
Model 12 (Aero)	9.14 × 10 ¹⁹	175	1.43 × 10 ⁻²	3.30 × 10 ⁻⁵	167.7	175.0	—

^aK_{max} is the maximum, asymptotic value of the K(r), while K₀ is the value adopted at 500 km.

sub-grid scale turbulence induced by unresolved vertically propagating gravity waves [cf. *Krasnopolsky, 2009*].

1.3. INMS Data

[11] As in parts 1 and 2, we compare T-GITM simulated densities and mixing ratios of N₂, CH₄, H₂, ⁴⁰Ar, and HCN to the measurements made by INMS, as determined by the data reduction methods of *Magee et al. [2009]*. Since we utilize a 1-D configuration of T-GITM, we take the INMS data between TA and T40 and combine them into a single, one-dimensional, mean profile with associated uncertainties (note that these uncertainties are not due to counting statistical errors, but are due to geophysical variations among the flybys). The details involved in generating these mean INMS data sets are provided by *Bell et al. [2010a]* and *Bell et al. [2010b]*. Figure 11 in part 1 illustrated that T-GITM simulations matching the INMS densities scaled up by a multiplicative factor of 3.0 best matched the combined temperature and density measurements made by the Huygens Atmospheric Science Instrument (HASI) and by the Composite Infrared Spectrometer (CIRS) [*Achterberg et al., 2008; Fulchignoni et al., 2005*]. Thus, we only consider T-GITM simulations that match the INMS data of *Magee et al. [2009]* scaled up by this uniform factor of 3.0.

2. The Mechanisms Determining the Vertical Methane Fluxes of T-GITM

[12] The works of *Bell et al. [2010a, 2010b]* established that the T-GITM methane homopause altitude significantly impacted the vertical methane escape fluxes required to reproduce the INMS measurements between TA and T40. Parts 1 and 2 used a series of T-GITM simulations with varying eddy diffusion profiles to illustrate this. Now, we demonstrate that, in addition to the homopause altitude, two other processes significantly modify the methane escape fluxes required by T-GITM: (1) the vertical momentum coupling between N₂ and CH₄, and (2) the column-integrated CH₄ chemical destruction. In order to accomplish this, we examine the different aspects of the simulated methane fluxes in Model 7 from *Bell et al. [2010b]*. We choose

Table 2. Settings at 1500 km for Models 7–12 (Aero)^a

	Φ _{CH₄} (molecules/m ² /s)	Methane Homopause (km)
Model 7	3.24 × 10 ¹²	950.0
Model 11	1.70 × 10 ¹³	880.0
Model 12	1.00 × 10 ¹⁰	985.0
Model 12 (NC)	1.00 × 10 ¹⁰	985.0
Model 12 (Aero)	1.00 × 10 ¹⁰	985.0

^aThe topside escape fluxes, Φ_{CH₄}, are referred to the surface of Titan.

this simulation because: (1) it matches the INMS data of *Magee et al. [2009]* scaled up by a factor of 3.0, (2) it does not include aerosol trapping, and finally (3) it does not rely upon ad hoc adjustments to the lower boundary ⁴⁰Ar mixing ratios relative to those measured by GCMS [*Niemann et al., 2005*].

[13] Although Model 7 is discussed in great detail by *Bell et al. [2010b]*, key fields from this simulation are presented in Figure 1, and the most salient lower boundary conditions are listed in Tables 1 and 2. Figure 1 compares both the simulated and the INMS ⁴⁰Ar mixing ratios in Figure 1a and the mixing ratios of CH₄ in Figure 1b. The percentage deviations between the INMS data and the Model 7 fields are given in Table 3. As seen in Table 2, Model 7 matches the INMS methane measurements of INMS with a CH₄ topside escape flux of 3.24 × 10¹² CH₄ m⁻² s⁻¹ (referred to the surface) using a methane homopause of 950 km.

[14] Having shown that Model 7 indeed reproduces the INMS data using reasonable lower boundary conditions, we next examine altitude profiles of the radial CH₄ fluxes simulated by Model 7 in Figures 2a and 2b, scaled so that they are referenced to the surface of Titan. Figure 2a depicts the vertical methane fluxes between 500 km and 1450 km, while Figure 2b highlights the same fluxes between 500 km and 700 km. Beginning at 500 km, the vertical methane fluxes increase with altitude up to a local maximum at 550 km, as shown more clearly in Figure 2b. Above 550 km, the vertical methane fluxes decrease with altitude until 850 km. Between 850 km and 900 km, the fluxes increase slightly, and, above 900 km, the vertical methane fluxes then decrease again until reaching an asymptotic value near 1450 km, which is the vertical escape flux of methane reported in Table 2 of 3.24 × 10¹² CH₄ m⁻² s⁻¹.

2.1. Reduced Momentum Equation

[15] Having examined the altitude profile of the CH₄ vertical fluxes in Model 7, we next investigate the dynamical terms in T-GITM that result in the variations noted above. Analyzing every term in the T-GITM vertical momentum equation is both unenlightening and cumbersome. In order to simplify this analysis, we consider a reduced form of the full vertical momentum equation by *Bell et al. [2010a]*, outlined in work by *Schunk and Nagy [2000]*, and given by

$$\Phi_s = -D_s n_s \left[\frac{1}{n_s} \frac{\partial n_s}{\partial r} + \frac{1}{T} \frac{\partial T}{\partial r} + \frac{1}{H_s} \right] - \frac{K n_s}{\chi_s} \frac{\partial \chi_s}{\partial r} + \frac{n_s}{N} \frac{D_s}{D_{sN_2}} \Phi_{N_2}. \quad (2)$$

In this expression, Φ_s is the vertical flux of methane, D_s is the total molecular diffusion coefficient for methane, D_{sN₂} is the

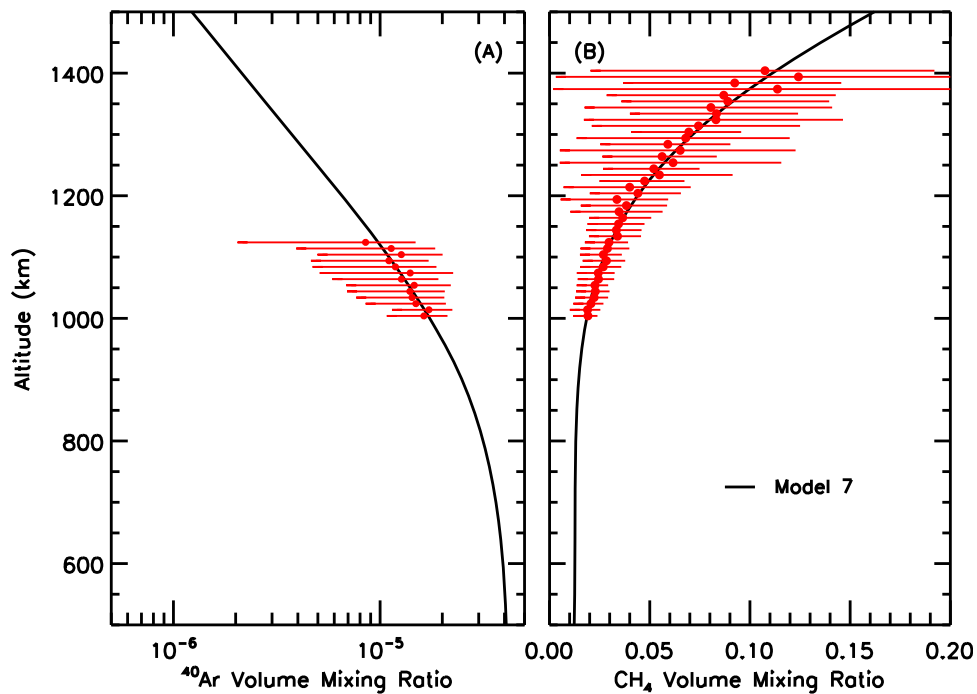


Figure 1. Simulated composition from Model 7. T-GITM fields are denoted by the black lines, while the average INMS data between TA and T40 are denoted by the red circles and associated horizontal uncertainties. (a) The simulated ^{40}Ar mixing ratios (black lines) compared against the INMS measurements (red circles) as determined by the methods of *Magee et al.* [2009] with associated uncertainties (horizontal red bars). (b) Simulated CH_4 volume mixing ratios compared against the INMS measurements.

$\text{CH}_4\text{-N}_2$ binary diffusion coefficient, N is the total density, T is the temperature, n_s is the density of methane, χ_s is the mole fraction of methane, K is the eddy diffusion coefficient, and Φ_{N_2} is the vertical flux of N_2 .

[16] This formula is derived directly from the T-GITM vertical momentum equation by *Bell et al.* [2010a] by eliminating the time-dependent terms, the gradients of velocity, and the sum over species in the momentum coupling terms. This expression retains only the $\text{CH}_4\text{-N}_2$ velocity coupling term in the form of Φ_{N_2} . Figures 3a and 3b depict the terms on the right-hand side of equation (2) for Model 7 of *Bell et al.* [2010b]. There are several curves on these plots and we enumerate them as follows: (1) red lines are the eddy diffusive fluxes ($\Phi^{E.D.}$) given by $-\frac{Kn_s}{\chi_s} \frac{\partial \chi_s}{\partial r}$; (2) blue lines are the molecular diffusive fluxes ($\Phi^{M.D.}$) given by $-D_s n_s \left[\frac{1}{n_s} \frac{\partial n_s}{\partial r} + \frac{1}{T} \frac{\partial T}{\partial r} + \frac{1}{H_s} \right]$; (3) grey lines represent the N_2 coupling fluxes (Φ^{N_2}) given by $\frac{n_s}{N} \frac{D_s}{D_{s\text{N}_2}} \Phi_{\text{N}_2}$; (4) magenta lines represent $\Phi^{E.D.} + \Phi^{M.D.}$; (5) yellow lines represent $\Phi^{E.D.} + \Phi^{M.D.} + \Phi^{\text{N}_2}$; (6) black lines represent the T-GITM vertical fluxes from Figure 2.

[17] First, we note that the actual CH_4 methane vertical fluxes (black curves) of Figure 2 and the approximation given by equation (2) (yellow curves) remain very consistent with one another. This indicates that equation (2) adequately approximates the dominant forces acting on methane in the T-GITM simulations. Note that the yellow curves in Figure 2a are a summation of the grey, red, and blue curves, while the yellow curves in Figure 2b are the combination of the grey and magenta curves.

[18] As seen in Figures 3a and 3b, the $\text{N}_2\text{-CH}_4$ interaction (grey curves) significantly modifies the overall vertical methane fluxes below the methane homopause altitude of 950 km. Above 950 km, the grey curve rapidly decreases to nearly 0.0, meaning that the collisional forces between N_2 and CH_4 do not extend much above the homopause, which is consistent with the transition from a well-mixed homosphere to a molecular diffusive heterosphere. In the lower atmosphere, these collisional forces can both locally enhance the vertical methane fluxes (positive values of the grey curve 600 km), and locally limit vertical methane fluxes (negative values of the grey curve between 700 km and 1450 km).

Table 3. Arithmetic Percent Deviations Between T-GITM and the INMS Measurements of *Magee et al.* [2009]^a

	N_2 Density	CH_4 Density	^{40}Ar Mixing Ratio	CH_4 Mixing Ratio	$^{14}\text{N}/^{15}\text{N}$ Ratio	$^{14}\text{N}/^{15}\text{N}$ Ratio (Below 1300 km)
Model 7	9.59	5.43	12.88	5.42	N/A	N/A
Model 11	7.00	5.77	34.00	4.60	5.10	6.70
Model 12	9.55	5.37	7.09	5.90	3.20	0.78
Model 12(NC)	10.00	6.00	7.08	5.90	3.30	0.77
Model 12(Aero)	11.00	5.50	7.98	5.90	3.59	0.94

^aThe “N/A” in Model 7 denotes that the $^{14}\text{N}/^{15}\text{N}$ ratio is not calculated for that simulation.

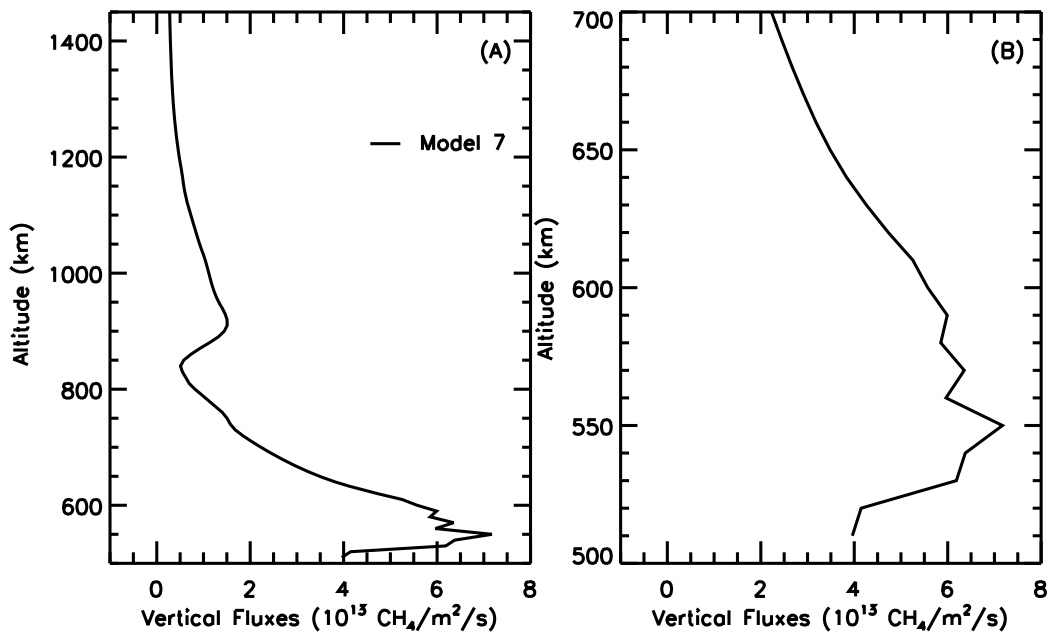


Figure 2. Vertical fluxes of methane from T-GITM Model 7. (a) Depiction of the vertical CH_4 fluxes between 500 km and 1450 km and (b) the lower altitudes between 500 km and 700 km.

[19] Next, we note in Figure 3a that the downward (i.e., negative) eddy diffusive fluxes (red curves) contribute significantly to the overall momentum balance at all altitudes, maximizing deep in the turbulent regime of the lower

thermosphere (below 800 km). These eddy diffusive fluxes are opposed by the upward molecular diffusive fluxes (blue curves), which represent another major component of the methane vertical momentum balance. Figure 3b combines

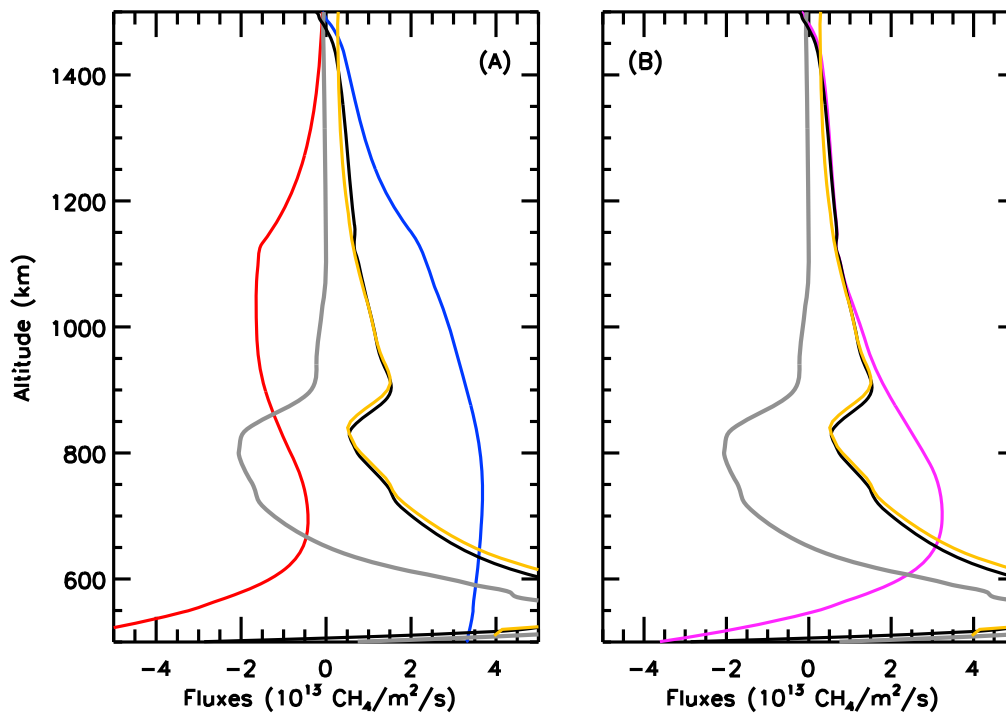


Figure 3. Key momentum balance terms for methane in Models 4 and 7. (a) The individual terms in equation (2) where (1) red lines are eddy diffusive fluxes, (2) blue lines are molecular diffusive fluxes, (3) grey lines are N_2 velocity coupling fluxes, (4) yellow is the combination of these three, and (5) the black lines are the CH_4 fluxes from Figure 2. (b) Combination of the red and blue lines into the magenta lines to highlight the importance of the N_2 momentum coupling (grey lines) separately.

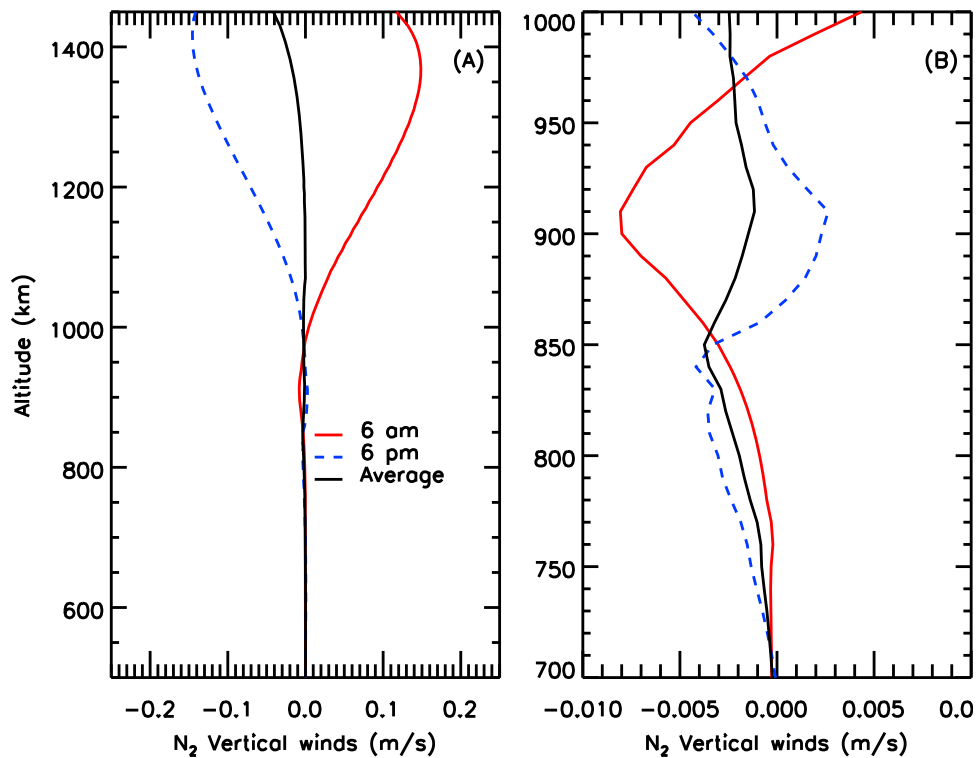


Figure 4. Nitrogen vertical winds from Model 7. (a) Winds between 500 km and 1450 km (similar to Figure 2), showing the morning terminator profile (red), the evening terminator profile (blue dashed), and the diurnal mean (black line). (b) The same curves, focusing on the altitude region (700 km–850 km) near the “bottleneck” in the CH₄ fluxes of Model 7.

the eddy diffusive and molecular diffusive fluxes into a single magenta curve. In this plot, we note that the vertical variations in the black and yellow curves (the full methane fluxes simulated by T-GITM) closely correlate with the variations in the grey curve. The variations in this grey curve are due to the vertical N₂ velocities, which are calculated in T-GITM from first principles.

[20] Figure 4 depicts the N₂ vertical winds simulated by Model 7 and there are 3 curves: (1) black lines represent the diurnal mean, (2) red lines represent the dawn terminator, and (3) blue dashed lines represent the dusk terminator. The nitrogen velocities exhibit upwelling on the dayside and downwelling on the nightside. Using the diurnally averaged speed of Nitrogen near the top of the model, we estimate that the net escape varies between $2.0\text{--}6.0 \times 10^{10} \text{ N}_2 \text{ m}^{-2} \text{ s}^{-1}$ (or $\sim 10^{24} \text{ N}_2/\text{s}$ globally) among the simulations. Figure 4b highlights these velocities between the altitudes of 700 and 1000 km. As shown in this plot, the diurnally averaged N₂ velocities reach a minimum value near 850 km (black line). This minimum correlates with the most negative values of the N₂–CH₄ coupling in Figures 3a and 3b. This suggests that the heavier background gas N₂ is locally limiting the upward flow of CH₄ in the homopause region.

2.2. CH₄ Mass Balance

[21] As shown in the last section, dynamical coupling between CH₄ and N₂ represents an important mechanism determining the local vertical methane fluxes simulated by T-GITM. However, as noted in Figure 2, the overall trend in the methane fluxes is to decrease with altitude from

the lower boundary at 500 km up to an asymptotic value near 1450 km. The only mechanism capable of irreversibly removing methane material from the atmosphere (besides atmospheric escape) is chemical destruction [cf. *Bell et al.*, 2010a, 2010b; *Strobel*, 2009; *Krasnopolsky*, 2009]. Figure 5 depicts an altitude profile of the total chemical destruction of methane in T-GITM Model 7. The details of the chemistry are given by *Bell et al.* [2010a], and, as shown in that work, the end product of the methane chemistry is the formation of C₂H₄, which is then transported down through the model lower boundary.

[22] In order to demonstrate the effects of CH₄ chemical destruction quantitatively, we employ a reduced version of the continuity equation, obtained after dropping the time-dependent terms to give

$$\nabla \cdot (\Phi_{CH_4}) = P_{CH_4} - L_{CH_4}. \quad (3)$$

In this expression, Φ_{CH_4} is the vertical methane flux and P_{CH_4} , L_{CH_4} are the methane chemical production and loss, respectively. Integrating this formula throughout the modeling domain, from $r_0 = 500$ km up to $r_{top} = 1500$ km, results in the following expression:

$$\Phi_{CH_4}(r_0) - \Phi_{CH_4}(r_{top}) = - \int_{r_0}^{r_{top}} (P_{CH_4} - L_{CH_4}) r^2 dr, \quad (4)$$

or, equivalently,

$$\Phi^{IN} + \int_{r_0}^{r_{top}} (P_{CH_4} - L_{CH_4}) r^2 dr = \Phi^{OUT}. \quad (5)$$

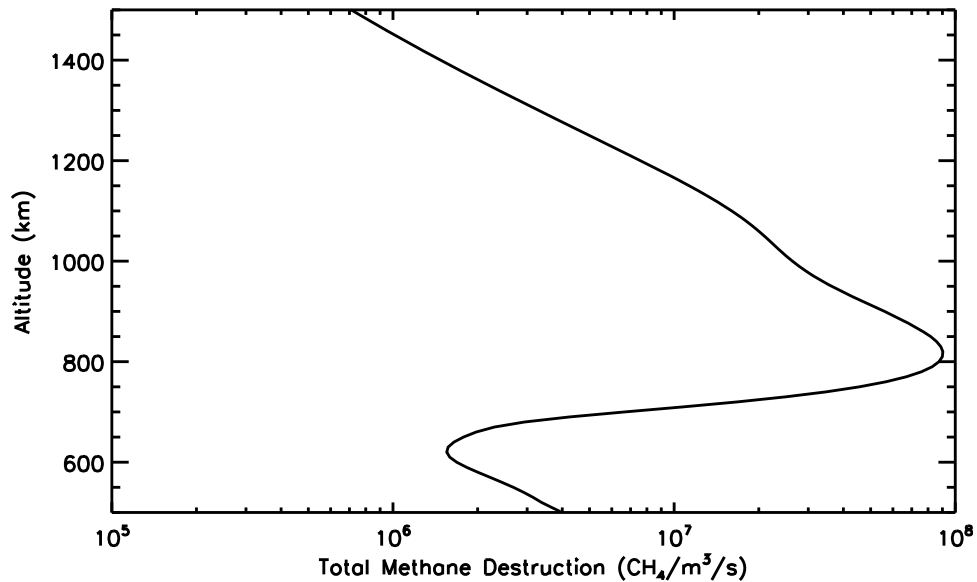


Figure 5. Altitude profile of the total chemical destruction of CH_4 present in Model 7.

Here, Φ^{IN} represents the upwelling methane fluxes from the lower atmosphere and Φ^{OUT} is the topside methane escape required by the model. Table 4 quantifies these terms in Model 7, showing that T-GITM satisfies this mass balance criterion (i.e., that $\Phi^{IN} + (\text{IntegratedChemicalLoss}) \sim \Phi^{OUT}$) to within $\sim 3\%$. This slight imbalance suggests that the time rate of change in the methane densities, which is omitted from equation (3), contributes roughly 3% to the total mass balance in this simulation.

[23] As seen in this table, the chemical destruction of methane in Model 7 is compensated by the upwelling of CH_4 material from the lower atmosphere. Figure 3 illustrates that the upwelling methane material is facilitated by: (1) momentum coupling with the N_2 vertical winds below 600 km and (2) through the combination of the eddy and molecular diffusive components in the vertical force balance. Most importantly, Table 4 reveals that, in addition to the dynamical mechanisms at work, the column-integrated destruction of methane represents a key factor in determining the topside escape rates required by T-GITM to reproduce INMS data.

2.3. Brief Summary

[24] Several studies have demonstrated that the vertical methane fluxes required to match INMS data are sensitively dependent upon the methane homopause altitude [cf. *Bell et al.*, 2010a, 2010b; *Strobel*, 2009; *Yelle et al.*, 2008]. In this section, we have demonstrated that, in addition to the homopause altitude, both the collisional interaction between CH_4 and N_2 and the column-integrated chemical destruction of methane are also integral to the T-GITM simulations. The

resulting vertical methane fluxes in Figure 2 possess significant variations with altitude.

[25] As demonstrated by Figure 3, the impacts of the N_2 - CH_4 coupling are significant at all altitudes below the homopause. Moreover, variations in the N_2 - CH_4 momentum coupling terms are tightly correlated with variations in the diurnally averaged N_2 vertical winds shown in Figure 4. As noted before, N_2 typically functions to limit the upward flow of methane, but it can also locally enhance the upward flow of methane, as it does in Figure 3 between 500 km and 600 km. Above the homopause, the N_2 - CH_4 coupling terms are significantly reduced, which is consistent with the transition from the collision-dominated lower thermosphere and the molecular diffusive upper thermosphere.

[26] The column-integrated chemical destruction of methane is also integral to simulating the vertical methane content in Titan's upper atmosphere, as demonstrated in section 2.2. The upwelling material through the model lower boundary is destroyed through chemical means, reducing the amount of material available at the upper boundary to escape. This suggests that increasing the chemical destruction of methane would result in a reduction in the topside escape fluxes of T-GITM required to reproduce INMS data, keeping all other parameters constant.

[27] However, it is important to note that the homopause altitude, the N_2 - CH_4 coupling, and the chemical destruction of methane are not completely independent. For instance, increasing the methane homopause altitude, allows the N_2 - CH_4 coupling to extend to higher altitudes. As seen in Figure 3, the net effect of the N_2 - CH_4 coupling near the homopause is to reduce or limit the upward flow of methane. Thus a higher

Table 4. Summary of CH_4 Mass Balance for Model 7^a

	Φ^{IN} ($\text{CH}_4/\text{m}^2/\text{s}$)	Integrated Chemical Loss ($\text{CH}_4/\text{m}^2/\text{s}$)	$\Delta\Phi$ ($\text{CH}_4/\text{m}^2/\text{s}$)	Φ^{OUT} ($\text{CH}_4/\text{m}^2/\text{s}$)
Model 7	3.939×10^{13}	-3.625×10^{13}	3.140×10^{12}	3.24×10^{12}

^a Φ^{IN} are the upward fluxes from the lower atmosphere, Φ^{OUT} are the escape methane fluxes from 1500 km, while $\Delta\Phi_{\text{CH}_4}$ is the difference between the upwelling fluxes and the column-integrated methane chemistry in that simulation (all referred to the surface of Titan).

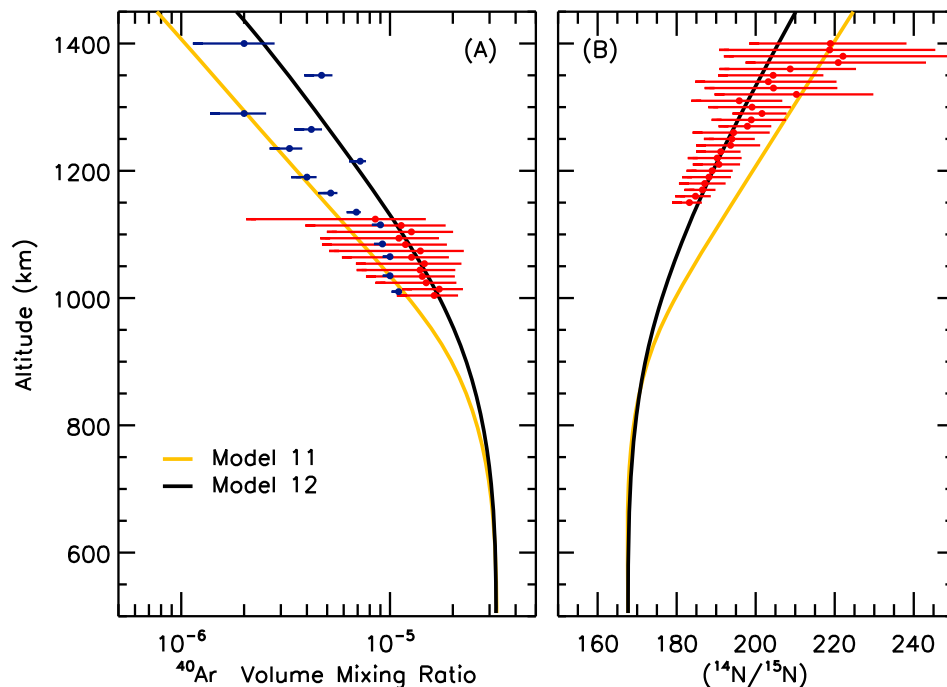


Figure 6. Results of the combined ^{40}Ar and $^{14}\text{N}/^{15}\text{N}$ analysis. (a) The T-GITM simulated ^{40}Ar abundances (black and yellow lines) are compared with those of *Magee et al.* [2009] (red) and *Yelle et al.* [2008] (blue). (b) A similar comparison between T-GITM simulated $^{14}\text{N}/^{15}\text{N}$ ratios and those of *Magee et al.* [2009] (in red). Note above 1300 km, the isotopes are not very reliable constraints on the homopause.

homopause allows N_2 to limit the upward flow of CH_4 over a larger region of the atmosphere. Simultaneously, adjustments to the homopause altitude will impact the eddy diffusive fluxes, modifying the simulated mixing ratios below the homopause. These modifications will then alter the local methane densities, impacting its local chemical destruction in the upper atmosphere. Hence, while one can treat these mechanisms as independent of one another, they are, in fact, highly coupled and their impacts cannot be separated in a trivial fashion.

3. Updated Constraints for Methane Escape

[28] As shown in the previous section, the homopause altitude, the N_2 – CH_4 coupling, and the total integrated chemical loss of methane represent equally important and mutually dependent processes that determine the escape of methane in T-GITM simulations matching the INMS data of *Magee et al.* [2009]. Now, we examine the impacts on the calculated methane homopause when we incorporate a recent re-analysis of the Huygens GCMS data by *Niemann et al.* [2010]. The latest GCMS analysis specifies the ^{40}Ar mixing ratio deep in the atmosphere to be $3.39 \pm 0.12 \times 10^{-5}$, which are roughly 20% below the previous value of $4.32 \pm 0.10 \times 10^{-5}$ in work by *Niemann et al.* [2005]. Moreover, *Niemann et al.* [2010] updated the isotopic $^{14}\text{N}/^{15}\text{N}$ ratio to 167.7 in the lower atmosphere, which we now use as an independent constraint for the methane homopause altitude (along with ^{40}Ar).

3.1. Updated ^{40}Ar and $^{14}\text{N}/^{15}\text{N}$ Measurements

[29] Using these updated constraints from GCMS, we now examine the impacts on the simulated vertical methane composition simulated by T-GITM. Figures 6 and 7 and

Tables 1 and 2 outline two new T-GITM simulations that match the updated GCMS composition constraints reported by *Niemann et al.* [2010]. These simulations are labeled Models 11 and 12 and they both match the INMS densities of *Magee et al.* [2009] scaled up by a factor of 3.0 with the lower boundary conditions in Table 1. The adjustments to the lower boundary conditions relative to Model 7 were required due to the imposition of the new GCMS constraints from *Niemann et al.* [2010]. Table 2 lists the methane homopause altitudes, and the required topside escape fluxes of Φ_{CH_4} . As found by *Bell et al.* [2010b], the lower methane homopause of 880 km in Model 11 necessitates high escape rates of $1.70 \times 10^{13} \text{ CH}_4 \text{ m}^{-2} \text{ s}^{-1}$ that must be imposed as upper boundary conditions in order to reproduce the INMS data. By contrast, the 985 km CH_4 homopause altitude in Model 12 allows T-GITM to match INMS using much lower methane escape rates.

[30] In order to better establish a proper homopause altitude for methane, we use two tracer species that are simultaneously measured by both GCMS and INMS: ^{40}Ar and the major isotope of N_2 , ^{14}N – $^{15}\text{N}_2$. While ^{40}Ar remains chemically inert and responds only to the combined interplay between molecular and eddy diffusion, ^{14}N – ^{15}N is a photochemically active species. Because of this, we must also include the enhanced photodissociation of this isotopic species outlined by *Liang et al.* [2007a]. However, rather than re-creating the detailed treatment of *Liang et al.* [2007a], we use a parameterization of the enhanced photodissociation rates from that previous work. We accomplish this by multiplying the calculated ^{14}N – ^{15}N photodissociation rates in T-GITM by a scaling factor (shown in Figure 8), which was taken from *Liang et al.* [2007a, Figure 2].

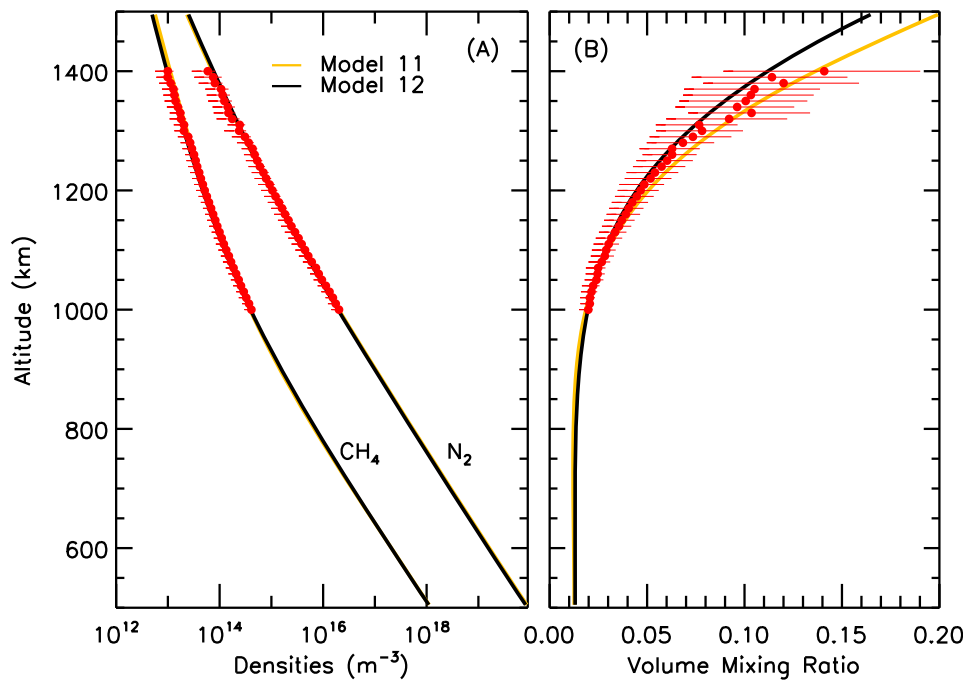


Figure 7. Results from the Nitrogen Isotope analysis. (a) The T-GITM simulated (black and yellow lines) major neutral densities of N_2 and CH_4 are compared with INMS data from *Magee et al.* [2009] (in red). (b) A comparison between T-GITM simulated CH_4 abundances and those of INMS.

[31] Key simulated fields from Models 11 and 12 are presented in Figures 6 and 7. In Figure 6a, the T-GITM simulated argon abundances are compared to relevant INMS data from *Yelle et al.* [2008] (blue circles) and *Magee et al.* [2009] (red circles). Yellow curves represent Model 11 and black curves denote Model 12 simulated fields. Similarly, in Figure 6b, we compare the T-GITM simulated $^{14}N/^{15}N$ ratios (yellow and black lines) to the INMS Nitrogen isotope ratio determined by *Magee et al.* [2009] and *Mandt et al.* [2009] (red circles and associated uncertainties).

[32] Figure 7 contains two plots that provide a similar comparison between T-GITM Models 11 and 12 to the INMS data determined by *Magee et al.* [2009]. In Figure 7a, the T-GITM simulated (black and yellow lines) neutral densities of N_2 and CH_4 are compared against the INMS data (red circles). Similarly, Figure 7b presents a comparison between T-GITM simulated CH_4 mixing ratios to the INMS composition (red circles). As can be seen in Figure 7, Models 11 and 12 visually match the INMS densities and mixing ratios determined by the methods of *Magee et al.* [2009] in

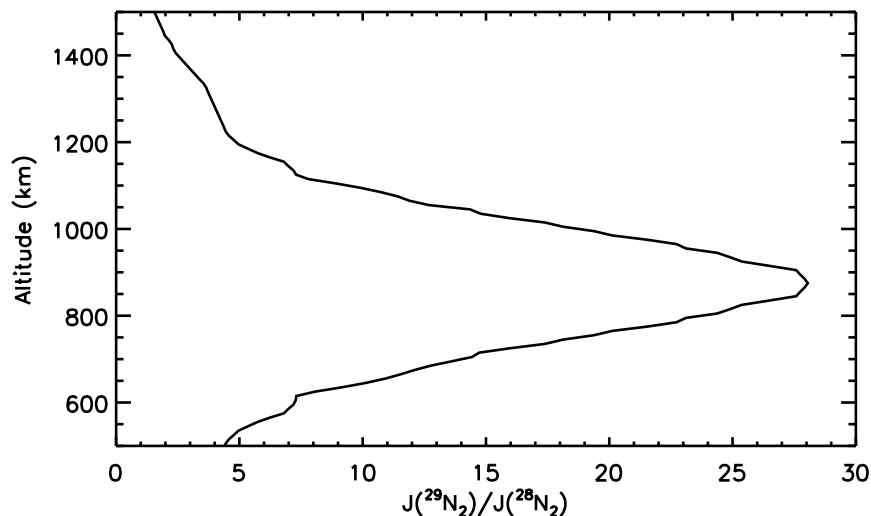


Figure 8. The ratio of photodissociation rate of the ^{15}N - ^{14}N isotope (denoted $^{29}N_2$) to that of the dominant ^{14}N - ^{14}N isotope (denoted $^{28}N_2$). This function is adapted from *Liang et al.* [2007a] and adjusted to account for the factor of 3.0 in densities (i.e., the peak of the photodestruction has been shifted up by a scale height).

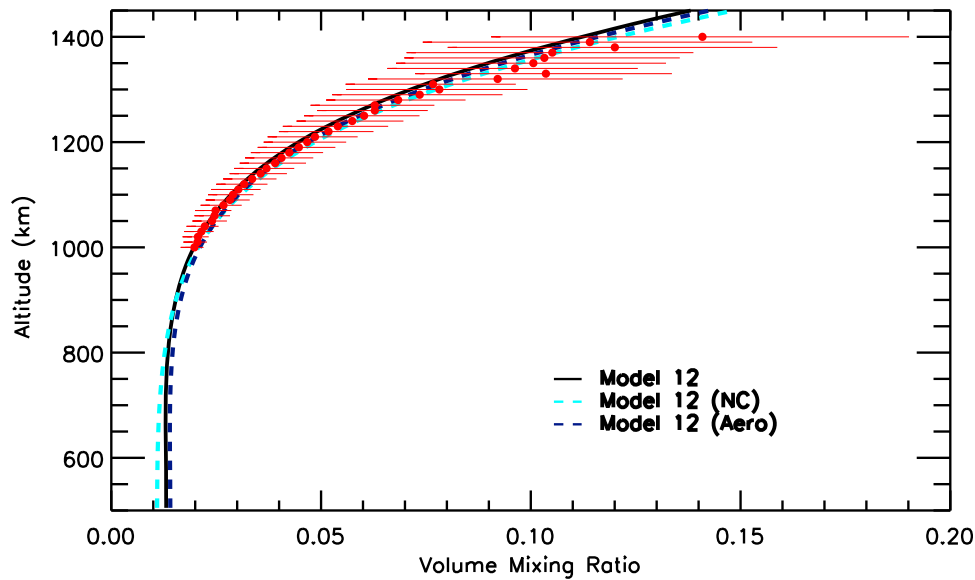


Figure 9. Results from adjusting the chemistry in T-GITM. Model 14 uses a lower boundary mixing ratio of 1.35%, while Model 14 (NC) must use a reduced methane mixing ratio of 1.1% to match INMS. Model 14 (Aero) includes additional aerosol trapping and uses a lower boundary methane mixing ratio of 1.43%.

a very similar fashion. Table 3 quantitatively corroborates this assessment, providing the arithmetic percent deviations between T-GITM and INMS data.

[33] Figure 6 and Table 3 indicate that there is a significant difference between the low methane homopause simulation (Model 11) and the higher methane homopause simulation (Model 12). Put simply, Model 11 is less consistent with INMS-determined $^{14}\text{N}/^{15}\text{N}$ ratios when using the GCMS-determined lower boundary condition of $^{14}\text{N}/^{15}\text{N} = 167.7$ [Niemann *et al.*, 2010]. By contrast, Model 12 simulates Nitrogen isotope ratios that are more consistent with the INMS-determined ratios. Despite the improved comparison, the T-GITM simulated isotope ratios diverge from the data above 1300 km. This divergence may be due to processes (such as horizontal transport) that are not accounted for by the 1-D T-GITM simulations. Future studies should examine the source of this apparent high-altitude discrepancy between the T-GITM simulated and the INMS measured $^{14}\text{N}/^{15}\text{N}$ ratios in more detail.

[34] Table 3 also demonstrates that Model 12 possesses the lowest percentage deviations from both the ^{40}Ar and Nitrogen isotopic ratios of Magee *et al.* [2009] and Mandt *et al.* [2009]. Furthermore, if one restricts the comparison to below 1300 km for the $^{14}\text{N}/^{15}\text{N}$ ratio, then Model 12 becomes even more compelling. By contrast, Model 11 (the low homopause case) fails to compare as well with the Nitrogen isotope below 1300 km. These findings suggest that the higher methane homopause altitude of ~ 1000 km in Model 12 remains preferable to that of 880 km in Model 11 on a “goodness of fit” basis. Furthermore, the low methane escape rates calculated by Model 12 remain more consistent with the combined CAPS and MIMI upper limits for neutral methane escape of roughly $1.1 \times 10^{11} \text{ CH}_4 \text{ m}^{-2} \text{ s}^{-1}$. For these reasons, Model 12 and its methane homopause altitude of 1000 km appears to be more consistent with the combined INMS and GCMS measurements.

3.2. Impacts of Altering the Methane Chemistry in T-GITM

[35] The last section demonstrated that the updated GCMS composition measurements of both ^{40}Ar and the $^{15}\text{N}/^{14}\text{N}$, combined with INMS measurements, imply a methane homopause of ~ 1000 km. As seen in Table 1, Model 11 and Model 12 both use different settings for the lower boundary mixing ratio of CH_4 , where Model 11 uses a 1.1% methane mixing ratio at 500 km and Model 12 uses a higher methane mixing ratio of 1.35% at 500 km. However, since the T-GITM lower boundary resides at 500 km, the methane mixing ratios in Models 11 and 12 should match the Huygens GCMS measurements by Niemann *et al.* [2010] ($1.48 \pm 0.09\%$). Thus, instead of using methane mixing ratios of 1.1% or 1.35% at the lower boundary, the model should be able to accommodate a mixing ratio within the range of GCMS and still reproduce the INMS data at higher altitudes.

[36] In this section, we demonstrate that alterations to the total column-integrated chemical destruction of methane allow us to modify the lower boundary methane mixing ratio of methane in T-GITM. By increasing the net chemical (or physico-chemical) destruction of methane, T-GITM can match INMS data, and impose higher methane mole mixing ratios at 500 km. By contrast, eliminating the methane chemical losses, requires that we reduce the methane mixing ratios significantly at 500 km. In order to demonstrate this, we now examine two new simulations, based upon Model 12: (1) a simulation that includes no chemical loss of methane, Model 12(NC); and (2) a simulation that includes an additional physico-chemical loss to aerosols, Model 12(Aero).

[37] All parameter settings in these two new simulations are identical to Model 12, except that Model 12(NC) omits the chemical destruction of methane and Model 12(Aero) adds a column-integrated aerosol trapping of $\sim 3.0 \times 10^{12}$

Table 5. Isolating the Impacts of Column-Integrated Total CH₄ Chemical Destruction (Referred to the Surface) and the Lower Boundary χ_{CH_4}

	χ_{CH_4} (%)	Column-Integrated CH ₄ Destruction (CH ₄ /m ² /s)
Model 12 (NC)	1.1	0.0
Model 12	1.35	3.65×10^{13}
Model 12 (Aero)	1.43	4.30×10^{13}

CH₄ m⁻² s⁻¹ (or, equivalently $\sim 8.0 \times 10^{-14}$ g cm⁻² s⁻¹). In order to maintain consistency with Model 12 and to limit the number of parameters that change, we have also maintained the same topside escape rate of methane for Models 12(NC) and 12(Aero). Finally, we note that, in Model 12(NC), T-GITM still calculates the chemical destruction of CH₄ to drive the formation of minor species; however, the model does not subtract this chemical destruction from the methane itself.

[38] The key settings for Models 12(NC) and 12(Aero) are shown in Tables 1 and 2, and we compare the resulting methane abundance profiles in Models 12, 12(NC), and 12(Aero) in Figure 9. Table 5 summarizes how altering the column-integrated destruction of methane impacts the lower boundary methane mixing ratios that can be used by the T-GITM simulations to reproduce the INMS data. As seen in this table, when keeping both the methane homopause and topside escape rates constant, T-GITM can accommodate higher methane mixing ratios at 500 km when using higher photochemical destruction of methane.

[39] In Model 12(NC), we *must* reduce the CH₄ mixing ratio settings at 500 km down to 1.1% in order to match the INMS measurements above 1000 km and keep the topside escape rates the same as those in Model 12. This required reduction in methane lower boundary mixing ratios can be explained by re-examining equation (2). According to equation (2) reducing the methane mixing ratio (and consequently n_s) deep in the atmosphere effectively “chokes off” the vertical flow of methane into the model, because the upward molecular diffusive fluxes of methane are directly proportional to the abundances of CH₄. The subsequent reduction in the upward methane fluxes in Model 12(NC) effectively offsets this simulation’s lack of CH₄ chemical loss.

[40] By contrast, Model 12, which includes 3.65×10^{13} CH₄ m⁻² s⁻¹ of methane destruction, can match INMS data while utilizing methane abundances of 1.35% at 500 km. Furthermore, after adding an additional 3.0×10^{12} CH₄ m⁻² s⁻¹ (referred to the surface) of column-integrated aerosol trapping, T-GITM Model 12 (Aero) can match the INMS data of Magee *et al.* [2009] using a lower boundary methane mixing ratio of 1.43%, which lies within the measurement range of GCMS ($1.48 \pm 0.09\%$) in work by Niemann *et al.* [2010].

Table 6. Parameters for the 1-D Hydrostatic Diffusion Model^a

	Settings at 100 km			Settings at 1500 km	
	Total Density (molecules/m ³)	K_0 (m ² /s)	⁴⁰ Ar Mixing Ratio	Φ_{CH_4} (molecules/m ² /s)	CH ₄ Homopause (km)
Model A	4.90×10^{23}	1.00	4.3×10^{-5}	3.05×10^{13}	848
Model B	4.90×10^{23}	3.50	3.3×10^{-5}	1.00×10^{10}	1001

^aThe CH₄ mixing ratio is set to 1.1% at 100 km. K_0 is the eddy diffusion coefficient at 100 km. Φ_{CH_4} is the methane escape flux imposed at 1500 km.

This additional destruction of methane need not necessarily come from aerosols. Any process that provides an additional 10% dissociation of methane over solar-driven chemistry (i.e., electron precipitation) can be used in place of aerosol trapping. However, the ubiquity of hazes and aerosols in Titan’s upper atmosphere makes aerosol trapping a compelling candidate for one such process [cf. Bar-Nun *et al.*, 2008; Liang *et al.*, 2007b].

4. 1-D Diffusion Model

[41] Section 3 examined the impacts of altering both the methane homopause and altering the column-integrated chemistry in T-GITM. Next, we investigate the results from a model that does not include the N₂-CH₄ coupling terms that are also identified as critical to T-GITM simulations. However since T-GITM is an inherently non-hydrostatic model, removing this critical piece of physics makes the resulting model less numerically stable and the results questionable. Thus, instead of attempting to recreate a new “hydrostatic GITM,” we next investigate the results from an independent, hydrostatic diffusion model that solves equation (2). This allows us to examine the impacts of removing this N₂-CH₄ coupling term from simulations of Titan’s upper atmosphere and provides an independent estimate for methane escape fluxes.

4.1. Diffusion Model Description

[42] In this section we outline the development of an independent, hydrostatic 1-D diffusion model that we use to reproduce the averaged INMS data of Magee *et al.* [2009]. This 1-D hydrostatic diffusion model numerically solves equation (2) between 100 km and 1500 km, after removing the influence of the N₂ vertical dynamics and ignoring methane chemical losses in the upper atmosphere (see Appendix A for the details). After these simplifications, one arrives at the following approximation for the vertical momentum equation:

$$\Phi_s = -D_s n_s \left[\frac{1}{n_s} \frac{\partial n_s}{\partial r} + \frac{1}{T} \frac{\partial T}{\partial r} + \frac{1}{H_s} \right] - \frac{K n_s}{\chi_s} \frac{\partial \chi_s}{\partial r}. \quad (6)$$

This can be re-written by isolating the gradient of the methane mixing ratio, χ_s , leading to the following expression [see Yelle *et al.*, 2008]:

$$\frac{1}{\chi_s} \frac{\partial \chi_s}{\partial r} = \frac{D_s}{D_s + K} \left[\frac{1}{H_{atm}} - \frac{1}{H_s} \right] \left(1 - \frac{\Phi_s}{\Phi_{l,s}} \right), \quad (7)$$

where we have introduced the limiting flux, $\Phi_{l,s} = D_s n_s \left(\frac{1}{H_{atm}} - \frac{1}{H_s} \right)$, the species-specific scale height $H_s = \frac{k_b T}{m_s g}$, and the mean atmospheric scale height given by $\frac{1}{H_{atm}} = \frac{m g}{k_b T} = \left(\frac{1}{N} \frac{\partial N}{\partial r} + \frac{1}{T} \frac{\partial T}{\partial r} \right)$ [Hunten, 1973].

Table 7. Arithmetic Percent Deviations Between the Diffusion Model Simulated Fields and the INMS Data From *Magee et al.* [2009]

	N ₂ Density	CH ₄ Density	⁴⁰ Ar Mixing Ratio	CH ₄ Mixing Ratio
Model A	8.61	7.40	22.22	6.55
Model B	8.60	7.39	11.37	6.11

4.2. Diffusion Model Results

[43] Using the diffusion model outlined above, we present two new simulations (Models A and B in Table 6) of Titan's upper atmosphere. Model A uses the methane and argon lower boundary conditions established in work by *Yelle et al.* [2008] in order to provide a direct comparison between this model and the previous hydrostatic diffusion model. Model A matches the ⁴⁰Ar of *Yelle et al.* [2008], which imposes a methane homopause altitude of ~840 km. Moreover, Model A provides a calibration benchmark simulation with respect to the work by *Yelle et al.* [2008], allowing us to immediately validate this new 1-D model.

[44] Model B is identical to Model A, except now, the updated GCMS argon mixing ratios are used at the lower boundary at 100 km and it matches the ⁴⁰Ar of *Magee et al.* [2009]. Using these constraints, Model B possesses a methane homopause of nearly 1000 km. Both hydrostatic simulations match the INMS densities of *Magee et al.* [2009] scaled up by a factor of 3.0 (Models A and B). Tables 6 and 7 contain the key boundary conditions and

error analysis, respectively, for these hydrostatic simulations. We note that both hydrostatic models impose a lower boundary methane mixing ratio of 1.1%, which is consistent with the lower boundary constraints required by the T-GITM Model 12 (NC).

[45] The results from Models A and B are presented in Figures 10–11 and in Tables 6 and 7. Figure 10 shows the vertical temperature profile used in the 1-D model in Figure 10a and the simulated total neutral densities in Figure 10b. In Figure 10a, the thermal structure between 100 km and 500 km is adapted from the CIRS measurements presented by *Teanby et al.* [2007]. Above 500 km, the temperatures in Figure 10 are taken from the T-GITM Model 7 thermal structure. Similarly, Figure 10b presents the simulated (black line) total neutral densities that match the INMS total densities of *Magee et al.* [2009] scaled up by a factor of 3.0 (yellow circles).

[46] Figure 11 contains the simulated mixing ratios from the diffusion model for the two simulations. Figure 11a, provides a comparison between the simulated ⁴⁰Ar mixing ratios of INMS, while Figure 11b depicts a similar comparison between the simulated CH₄ mixing ratio and those of INMS. The percent deviations between the INMS data and diffusion model fields are provided in Table 7, illustrating quantitatively that each hydrostatic simulation reproduces N₂ and CH₄ densities and mixing ratios equivalently well on a goodness-of-fit basis. Note that, in this table, the Model A ⁴⁰Ar abundances are compared with those of *Yelle et al.* [2008], while Model B ⁴⁰Ar abundances

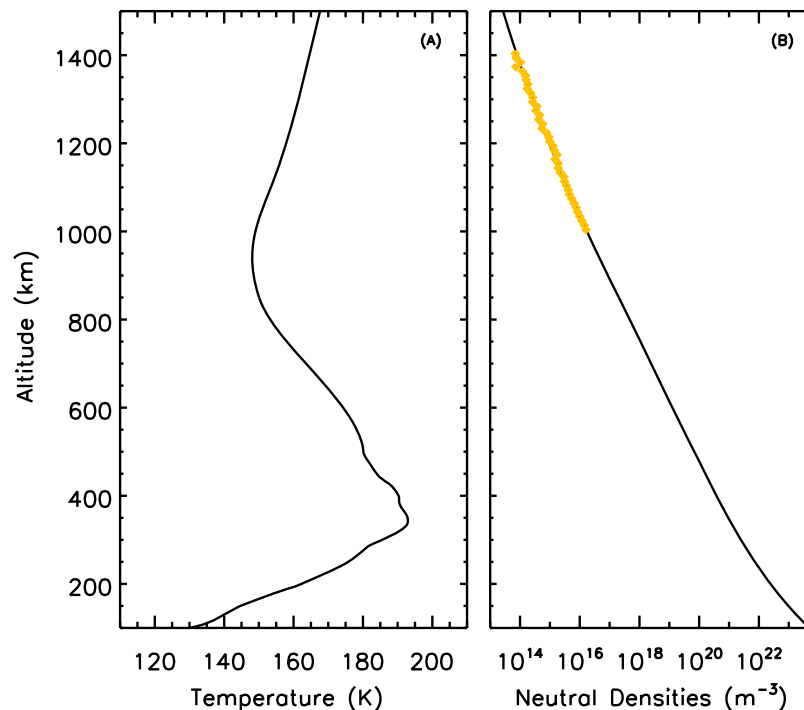


Figure 10. Temperatures and total densities in the hydrostatic model. (a) The imposed and unchanging thermal structures used for the simulations matching the unscaled INMS densities (solid line) and those matching the INMS densities scaled up by a factor of 3.0 (dashed line). (b) The resulting total neutral densities, where the blue circles represent the INMS densities of *Magee et al.* [2009] and the yellow circles represent those densities multiplied by 3.0.

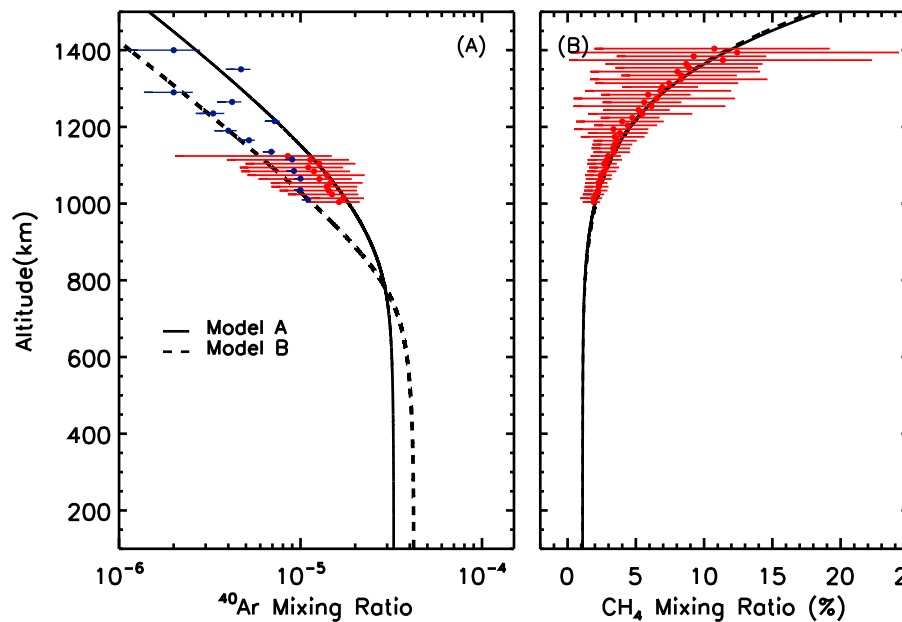


Figure 11. 1-D hydrostatic diffusion model composition results for the cases matching the unscaled INMS densities of *Magee et al.* [2009]. (a) The simulated ^{40}Ar abundances (black and grey lines) and the INMS results from *Magee et al.* [2009] (red circles) and *Yelle et al.* [2008] (blue circles). (b) The model simulated CH_4 abundances compared with those of *Magee et al.* [2009] (red circles).

are compared to those of *Magee et al.* [2009]. The topside escape fluxes of methane required by the hydrostatic model are provided in Table 6.

[47] The results from this simplified hydrostatic diffusion model are illustrative in several respects. First, Model A requires methane escape rates of $3.05 \times 10^{13} \text{ CH}_4 \text{ m}^{-2} \text{ s}^{-1}$ to reproduce INMS methane composition and imposes a methane homopause altitude of ~ 840 km. Using almost identical constraints, *Yelle et al.* [2008] inferred methane escape rates between $2.5\text{--}3.0 \times 10^{13} \text{ CH}_4 \text{ m}^{-2} \text{ s}^{-1}$ are required to reproduce INMS data using a homopause at 840 km. We note that the study by *Yelle et al.* [2008] utilizes a different thermal and density structure, since they were matching the unscaled INMS densities, and this may explain why the hydrostatic model of this study infers methane fluxes that are roughly 15% higher than the previous study. The close agreement between Model A and *Yelle et al.* [2008] indicates that this model is consistent with that earlier work and provides a validation for the approach taken here.

[48] By contrast, Model B uses the updated GCMS ^{40}Ar constraints from *Niemann et al.* [2010], which places the methane homopause location at roughly 1000 km, and it requires methane escape rates of $1.0 \times 10^{10} \text{ CH}_4 \text{ m}^{-2} \text{ s}^{-1}$ to reproduce INMS data. These lower escape rates in Model B fall within the upper limits inferred from CAPS and MIMI observations ($1.1 \times 10^{10} \text{ molecules m}^{-2} \text{ s}^{-1}$). This result is very similar to that of Model 12(NC), indicating that T-GITM and the hydrostatic diffusion model are also in excellent agreement under similar parameter settings and when ignoring methane chemistry. This further demonstrates that the high-homopause, low escape rate scenario for reproducing INMS methane observations is not unique

to T-GITM, and it can be reproduced by an independent 1-D hydrostatic model.

5. Discussion and Analysis

[49] In section 2, we outline three fundamental parameters and processes that are critical to determining the vertical methane fluxes in the Titan GITM framework: (1) the methane homopause altitude, (2) the $\text{N}_2\text{--CH}_4$ coupling, and (3) the total column integrated chemical (and physico-chemical) destruction of methane. Figures 2 through 4 illustrate the interplay between these three core aspects of T-GITM. First the homopause altitude, once set, determines the extent of the homosphere in T-GITM and the magnitude of the eddy diffusive fluxes in Figure 3. Simultaneously, changing the methane homopause altitude alters the altitudes over which N_2 can modify the upward flow of methane (see grey curves in Figure 3). Similarly, altering the homopause will also vary the local CH_4 densities (mixing ratios) at high altitudes, subsequently modifying its vertical chemical destruction.

[50] In section 3, we first examined the implications of the updated analysis of the GCMS data by *Niemann et al.* [2010], who reported a modified ^{40}Ar mixing ratio of $3.39 \pm 0.12 \times 10^{-5}$ and an updated $^{14}\text{N}/^{15}\text{N}$ ratio of 167.7. Using these two metrics, in addition to the INMS data reduced by *Magee et al.* [2009], we conclude that a homopause of ~ 1000 km is necessitated to accurately reconcile measurements of both ^{40}Ar and the $^{15}\text{N}/^{14}\text{N}$ ratio by both instruments. This is the first attempt at using multiple minor species to constrain the methane homopause altitude at Titan, and both species give a consistent answer. Using a methane homopause altitude of 1000 km, the T-GITM simulation Model 12 reproduces the INMS methane using a methane of escape flux

of $1.0 \times 10^{10} \text{ CH}_4 \text{ m}^{-2} \text{ s}^{-1}$, which is consistent with both CAPS and MIMI observations in the magnetosphere.

[51] However, despite the ability of Model 12 to reconcile GCMS, INMS, HASI, CIRS, CAPS, and MIMI measurements, it must still use a lower boundary mixing ratio of 1.35%, which is lower than the range of GCMS measurements, which are $1.48 \pm 0.09\%$ [Niemann *et al.*, 2010]. We next demonstrate that, by adding an additional loss of methane equivalent to $3.0 \times 10^{12} \text{ CH}_4 \text{ m}^{-2} \text{ s}^{-1}$ (referred to the surface), the T-GITM simulation Model 12 (Aero) could then replicate the INMS data using a lower boundary methane mixing ratio of 1.43 % (while using methane escape rates consistent with CAPS and MIMI).

[52] This additional chemical loss of methane amounts to only a 10% correction to the column-integrated photochemical destruction of methane in T-GITM, which ranges between $3.625\text{--}4.30 \times 10^{13} \text{ CH}_4 \text{ m}^{-2} \text{ s}^{-1}$ (see Tables 4 and 5). While a direct comparison with T-GITM estimates is unavailable (i.e., no other photochemical study has explicitly focused on the altitude region above 500 km), other investigations have estimated integrated chemical destruction of methane from the surface up to the exobase ranging between $5.0 \times 10^{13} \text{ CH}_4 \text{ m}^{-2} \text{ s}^{-1}$ in work by Wilson and Atreya [2004] up to $1.5 \times 10^{14} \text{ CH}_4 \text{ m}^{-2} \text{ s}^{-1}$ in work by Yung *et al.* [1984]. Hence, the additional aerosol trapping/adsorption suggested in Model 12 (Aero) of $3.0 \times 10^{12} \text{ CH}_4 \text{ m}^{-2} \text{ s}^{-1}$ would amount to between a 2–6% enhancement to the global destruction of methane [cf. Mandt *et al.*, 2009]. Moreover, this additional loss need not come solely from aerosols, and other processes (such as electron impact dissociation) could also contribute significantly.

[53] Finally, in section 4 we demonstrated that the T-GITM results could be replicated by an independent, hydrostatic diffusion model that neglected both (1) the $\text{N}_2\text{--CH}_4$ coupling and (2) chemical destruction of methane. Comparing the diffusion Model B to Model 12 (NC) illustrates that both models, in large part, are in agreement with one another. Both models use a reduced methane mixing ratio of 1.1% deep in the atmosphere and both reproduce the INMS methane measurements with low escape rates. This forced reduction in the methane mole mixing ratio at the lower boundary of both Model 12 (NC) and Model B remains inconsistent with GCMS, and it is due to the omission of methane chemistry (see Table 5).

[54] Ultimately, we have demonstrated that: (1) the methane homopause altitude is most likely 1000 km, (2) using this homopause, vertical escape fluxes of methane of $1.0 \times 10^{10} \text{ CH}_4 \text{ m}^{-2} \text{ s}^{-1}$ can match the INMS data when using GCMS constraints, and (3) these results are independent of the model employed. Moreover, we have shown that other methane loss processes, such as aerosol trapping [Bar-Nun *et al.*, 2008], allows T-GITM to match INMS data using a lower boundary methane mixing ratio of 1.43%, which lies within the measurement uncertainties of GCMS [Niemann *et al.*, 2010]

6. On the Possibilities and Probabilities of Hydrodynamic Escape of Methane

[55] Early work by both Yelle *et al.* [2008] and Strobel [2009] (and later by Strobel [2010]) have suggested that hydrodynamic escape *is required* to reproduce INMS meth-

ane densities and composition. However, no work to date has been able to reconcile these escape rates ($2.0\text{--}2.8 \times 10^{13} \text{ CH}_4 \text{ m}^{-2} \text{ s}^{-1}$) with near-Titan carbon ion estimates by CAPS and MIMI, both of which place an upper limit to neutral carbon outflow at $1.0\text{--}2.0 \times 10^{11} \text{ CH}_4 \text{ m}^{-2} \text{ s}^{-1}$. Moreover, hydrodynamic escape is typically defined as the bulk outflow of an atmosphere [cf. Tian *et al.*, 2008], which stabilizes atmospheres from an unstable “blowoff” state. Thus, in a truly hydrodynamic scenario, one would expect that all major constituents would be flowing outward according to their abundances near the exobase.

[56] However, in the scenario posited by Strobel [2009, 2010] and Yelle *et al.* [2008], only CH_4 is hydrodynamically escaping Titan's upper atmosphere. Meanwhile N_2 is assumed to be static (i.e., 0.0 velocities at all altitudes). Additionally, after incorporating the factor of 3.0 into the INMS density data of Magee *et al.* [2009], H_2 INMS data can be reproduced by T-GITM using Jeans escape alone [see Bell *et al.*, 2010a, 2010b]. Thus, in order to support the hydrodynamic escape hypothesis for methane, one must invoke a mechanism that selectively energizes the relatively heavy constituent CH_4 , while not impacting either the more abundant N_2 or the lightest gas H_2 .

[57] Furthermore, other modeling studies, such as Bell *et al.* [2010a, 2010b] and Tucker and Johnson [2009] have not been able to drive the atmosphere of Titan into a hydrodynamic escape regime, regardless of additional inputs of energy. The studies by Bell *et al.* [2010a, 2010b] employ the non-hydrostatic GITM framework, which has been shown to simulate enhanced vertical flows in response to localized heating events at Earth [cf. Deng *et al.*, 2008]. Similarly, the Direct Simulation Monte Carlo (DMSC) technique of Tucker and Johnson [2009] is capable of generating enhanced escape rates from both thermal and non-thermal processes. Despite this, neither the non-hydrostatic Navier-Stokes model, nor the kinetic model can reproduce hydrodynamic methane escape self-consistently at Titan. Thus, if one were to prefer the hydrodynamic escape hypothesis to explain Titan's upper atmosphere, then there are three major aspects to that require further study: (1) why do the data sets in the magnetosphere (i.e., CAPS and MIMI) refute its predictions? (i.e., why does 99% of the neutral methane leave no ion signature in the magnetosphere?); (2) Why can't other models capable of predicting non-hydrostatic outflows from planetary atmospheres reproduce it self-consistently (without simply imposing it as a boundary condition?); (3) Finally, why is methane alone energized by these processes while N_2 is left static and H_2 simply escapes with Jeans escape speeds?

[58] However, as we have shown in this study, there is a more straight-forward alternative to the hydrodynamic escape hypothesis that reproduces that INMS data equivalently well, while also remaining consistent with HASI, CIRS, GCMS, CAPS, and MIMI. Using updated GCMS and INMS determinations of the ^{40}Ar abundances and $^{14}\text{N}/^{15}\text{N}$ ratios, we have found that the methane homopause is most likely at 1000 km. And, using this homopause altitude, we can: (1) use lower atmospheric constraints from multiple instruments (HASI, CIRS, GCMS), (2) use low methane escape rates consistent with CAPS and MIMI, and (3) reproduce all the major species measured by INMS between TA and T40 to within 10%. This configuration is also consistent with the previous estimates of the methane homopause altitude

inferred by *Vervack et al.* [2004] using Voyager data and by *De La Haye et al.* [2008] during the initial analysis of the INMS TA data. Moreover, this low escape scenario remains consistent with kinetic models of the thermosphere–exosphere [Tucker and Johnson, 2009] and with hydrostatic diffusion models of Titan's upper atmosphere [cf. *Krasnopolsky, 2010; De La Haye et al., 2008*].

Appendix A: 1-D Diffusion Model Formulation

[59] In order to develop the one-dimensional (1-D) hydrostatic diffusion model, we take the Navier–Stokes continuity and momentum equations from *Bell et al.* [2010a], and omit all of the time-derivative terms and any non-linear terms, such as the stress tensor, material derivatives, and so on. Essentially, we need only look at equation (2) and drop the last term on the right hand side. Furthermore, we remove any thermal structure calculations by specifying a fixed temperature. Simplifying matters, we neglect chemical calculations. Finally, for ease of comparison with recent work, we re-cast the reduced continuity and momentum equations in a way commensurate with *Yelle et al.* [2008].

[60] Using the simplifying assumptions outlined above, the Navier–Stokes equations of part 1 are reduced to the following: 1. Continuity:

$$\nabla \cdot (\Phi_s) = 0, \quad (\text{A1})$$

2. Momentum:

$$\frac{1}{\chi_s} \frac{\partial \chi_s}{\partial r} = \frac{D_s}{D_s + K} \left[\frac{1}{H_{atm}} - \frac{1}{H_s} \right] \left(1 - \frac{\Phi_s}{\Phi_{l,s}} \right), \quad (\text{A2})$$

3. Diffusion Limited Flux:

$$\Phi_{l,s} = D_s N \left(\frac{1}{H_{atm}} - \frac{1}{H_s} \right) \chi_s. \quad (\text{A3})$$

4. Hydrostatic Equilibrium of the atmosphere:

$$\frac{1}{N} \frac{\partial N}{\partial r} + \frac{1}{T} \frac{\partial T}{\partial r} = - \left(\frac{1}{H_{atm}} \right). \quad (\text{A4})$$

In these expressions, Φ_s is the species-specific flux (in molecules/m²/s), where $\Phi_s = n_s v_s$ and $\Phi_{l,s}$ represents the diffusion limited flux of *Hunten* [1973]. H_{atm} is the atmospheric scale height (in m) and H_s is the species-specific scale height. D_s represents the total diffusion coefficient for species “s” (in m²/s) and K is the turbulent diffusion coefficient. Finally, χ_s is the volume mixing ratio for species “s”, defined by $\chi_s = n_s/N$, where n_s is the species density and N is the total density.

[61] Equations (A1)–(A4) form the basis for the 1-D diffusion model that can be explicitly integrated on a uniform radial grid centered on Titan using the Interactive Data Language (IDL). The continuity equation does not require numerical integration and can be solved analytically. By integrating from a level, r , up to the top of the atmosphere in spherical polar coordinates, one obtains

$$\int_r^{r_{top}} 0 \, dr = \alpha = \int_r^{r_{top}} \frac{\partial}{\partial r} (r^2 \Phi_s) \, dr = r_{top}^2 \Phi_s(r_{top}) - r^2 \Phi_s(r). \quad (\text{A5})$$

In this expression, α is merely the constant of integration, which by setting $r = r_{top}$, we see that $\alpha = 0$. This gives us an alternative statement of the continuity equation:

$$\Phi_s(r) = \left(\frac{r_{top}}{r} \right)^2 \Phi_{top}. \quad (\text{A6})$$

[62] This last expression merely states that, when ignoring chemistry, the vertical fluxes through a spherical surface must be conserved. The r^2 accounts for the variation of the surface area of a sphere with radius. We next numerically solve equations (A2), (A3) (A4), and (A6) in an iterative fashion, using 1 km radial grid that extends from 100 km to 1500 km above Titan's surface. We only solve these equations for CH₄, ⁴⁰Ar, and N₂. Moreover, we assume that the $\Phi_s = 0$ for both N₂ and ⁴⁰Ar, in analogy with *Yelle et al.* [2008]. We specify the fluxes for CH₄ at the top of the model, in order to match the INMS mixing ratios and densities. In order to numerically integrate equations (A2) and (A4), we make use of a 5th order Newton–Cotes formulation, which is readily available as a prepackaged routine in IDL.

[63] In addition to directly integrating these equations, we also iterate our solution. For each iteration, we compare our results of the updated variables with those of the previous iteration. In order to define a convergence criteria, we chose to iterate the solution until the maximum difference in the volume mixing ratios of N₂, ⁴⁰Ar, and CH₄ between iterations was less than 1×10^{-10} . The iterative procedure that we follow is (1) solve for N, using equation (A4); (2) solve χ_{CH_4} and $\chi_{^{40}Ar}$, using equations (A2), (A3), and (A6); (3) update n_{CH_4} and $n_{^{40}Ar}$ from Steps 1 and 2 above; (4) calculate $n_{N_2} = N - n_{CH_4} - n_{^{40}Ar}$; (5) update secondary variables (i.e., D_s , K , H_{atm}); (6) evaluate convergence of χ_{CH_4} and $\chi_{^{40}Ar}$ with previous iteration. As noted above, at the end of each iteration, we compute the maximum differences between the simulated mixing ratios of the current iteration from the previous iteration for all species. This difference is defined as

$$\text{Difference} = \max \left(\frac{|\chi_s^n - \chi_s^{n-1}|}{\chi_s^{n-1}} \right). \quad (\text{A7})$$

Here, χ_s^{n-1} denotes the value from the previous iteration, while χ_s^n represents the value from the current iteration. We take the maximum differences among the mixing ratios of CH₄, N₂, and ⁴⁰Ar and compare it with a tolerance value of 1.0×10^{-10} . We reach this level of convergence easily within 10–11 iterations.

[64] **Acknowledgments.** This work was supported by the NASA grant NAS703001NM0710023, subcontracted through the Jet Propulsion Laboratory (JPL). J. Bell would also like to thank the Center for Space Environment Modeling (CSEM) at the University of Michigan for continued access and use of their computational facilities and expertise. Lastly, the authors thank the staff at both the NASA High End Computing (HEC) and the Texas Advanced Computing Center (TACC) for use of their large scale computing facilities.

References

- Achterberg, R. K., B. J. Conrath, P. J. Gierasch, F. M. Flasar, and C. A. Nixon (2008), Titan's middle-atmospheric temperatures and dynamics observed by the Cassini Composite Infrared Spectrometer, *Icarus*, 194, 263–277, doi:10.1016/j.icarus.2007.09.029.
- Atreya, S. K. (1986), *Atmospheres and Ionospheres of the Outer Planets and Their Satellites*, *Phys. Chem. Space*, vol. 15, Springer, Berlin.

- Bar-Nun, A., V. Dimitrov, and M. Tomasko (2008), Titan's aerosols: Comparison between our model and DISR findings, *Planet. Space Sci.*, *56*, 708–714, doi:10.1016/j.pss.2007.11.014.
- Bell, J. M., et al. (2010a), Simulating the one-dimensional structure of Titan's upper atmosphere: 1. Formulation of the Titan Global Ionosphere-Thermosphere Model and benchmark simulations, *J. Geophys. Res.*, *115*, E12002, doi:10.1029/2010JE003636.
- Bell, J. M., et al. (2010b), Simulating the one-dimensional structure of Titan's upper atmosphere: 2. Alternative scenarios for methane escape, *J. Geophys. Res.*, *115*, E12018, doi:10.1029/2010JE003638.
- Bell, J. M., J. Westlake, and J. H. Waite Jr. (2011), Simulating the time-dependent response of Titan's upper atmosphere to periods of magnetospheric forcing, *Geophys. Res. Lett.*, *38*, L06202, doi:10.1029/2010GL046420.
- Crary, F. J., H. T. Smith, D. Reisenfeld, and D. T. Young (2010), Upper limits on carbon group ions near the orbit of Titan: Implications for methane escape from Titan, paper presented at the 38th Scientific Assembly, Comm. on Space Res., Bremen, Germany, 15–18 July.
- De La Haye, V., J. H. Waite, T. E. Cravens, I. P. Robertson, and S. Lebonnois (2008), Coupled ion and neutral rotating model of Titan's upper atmosphere, *Icarus*, *197*, 110–136, doi:10.1016/j.icarus.2008.03.022.
- Deng, Y., A. D. Richmond, A. J. Ridley, and H.-L. Liu (2008), Assessment of the non-hydrostatic effect on the upper atmosphere using a general circulation model (GCM), *Geophys. Res. Lett.*, *35*, L01104, doi:10.1029/2007GL032182.
- Fulchignoni, M., et al. (2005), *In situ* measurements of the physical characteristics of Titan's environment, *Nature*, *438*, 785–791, doi:10.1038/nature04314.
- Hunten, D. M. (1973), The escape of H₂ from Titan, *J. Atmos. Sci.*, *30*, 726–732.
- Krasnopolsky, V. A. (2009), A photochemical model of Titan's atmosphere and ionosphere, *Icarus*, *201*, 226–256, doi:10.1016/j.icarus.2008.12.038.
- Krasnopolsky, V. A. (2010), The photochemical model of Titan's atmosphere and ionosphere: A version without hydrodynamic escape, *Planet. Space Sci.*, *58*, 1507–1515, doi:10.1016/j.pss.2010.07.010.
- Liang, M.-C., A. N. Heays, B. R. Lewis, S. T. Gibson, and Y. L. Yung (2007a), Source of nitrogen isotope anomaly in HCN in the atmosphere of Titan, *Astrophys. J.*, *664*, L115–L118, doi:10.1086/520881.
- Liang, M.-C., Y. L. Yung, and D. E. Shemansky (2007b), Photolytically generated aerosols in the mesosphere and thermosphere of Titan, *Astrophys. J.*, *661*, L199–L202, doi:10.1086/518785.
- Magee, B. A., J. H. Waite, K. E. Mandt, J. Westlake, J. Bell, and D. A. Gell (2009), INMS-derived composition of Titan's upper atmosphere: Analysis methods and model comparison, *Planet. Space Sci.*, *57*, 1895–1916, doi:10.1016/j.pss.2009.06.016.
- Mandt, K. E., J. H. Waite, W. Lewis, B. Magee, J. Bell, J. Lunine, O. Mouis, and D. Cordier (2009), Isotopic evolution of the major constituents of Titan's atmosphere based on Cassini data, *Planet. Space Sci.*, *57*, 1917–1930, doi:10.1016/j.pss.2009.06.005.
- Niemann, H. B., et al. (2005), The abundances of constituents of Titan's atmosphere from the GCMS instrument on the Huygens probe, *Nature*, *438*, 779–784, doi:10.1038/nature04122.
- Niemann, H. B., S. K. Atreya, J. E. Demick, D. Gautier, J. A. Haberman, D. N. Harpold, W. T. Kasprzak, J. I. Lunine, T. C. Owen, and F. Raulin (2010), The composition of Titan's lower atmosphere and simple surface volatiles as measured by the Cassini-Huygens probe gas chromatograph mass spectrometer experiment, *J. Geophys. Res.*, *115*, E12006, doi:10.1029/2010JE003659.
- Schunk, R., and A. F. Nagy (2000), *Ionospheres*, Cambridge Univ. Press, Cambridge, U. K.
- Smith, H. T., R. E. Johnson, M. E. Perry, A. M. Rymer, and T. A. Cassidy (2009), The influence of neutrals on Saturn's magnetosphere, paper presented at Magnetospheres of the Outer Planets, Univ. of Cologne, Cologne, Germany, 27–31 July.
- Strobel, D. F. (2008), Titan's hydrodynamically escaping atmosphere, *Icarus*, *193*, 588–594, doi:10.1016/j.icarus.2007.08.014.
- Strobel, D. F. (2009), Titan's hydrodynamically escaping atmosphere: Escape rates and the structure of the exobase region, *Icarus*, *202*, 632–641, doi:10.1016/j.icarus.2009.03.007.
- Strobel, D. F. (2010), Molecular hydrogen in Titan's atmosphere: Implications of the measured tropospheric and thermospheric mole fractions, *Icarus*, *208*, 878–886, doi:10.1016/j.icarus.2010.03.003.
- Teanby, N. A., et al. (2007), Vertical profiles of HCN, HC₃N, and C₂H₂ in Titan's atmosphere derived from Cassini/CIRS data, *Icarus*, *186*, 364–384, doi:10.1016/j.icarus.2006.09.024.
- Tian, F., J. F. Kasting, H. Liu, and R. G. Roble (2008), Hydrodynamic planetary thermosphere model: 1. Response of the Earth's thermosphere to extreme solar EUV conditions and the significance of adiabatic cooling, *J. Geophys. Res.*, *113*, E05008, doi:10.1029/2007JE002946.
- Tucker, O. J., and R. E. Johnson (2009), Thermally driven atmospheric escape: Monte Carlo simulations for Titan's atmosphere, *Planet. Space Sci.*, *57*, 1889–1894, doi:10.1016/j.pss.2009.06.003.
- Vervack, R. J., B. R. Sandel, and D. F. Strobel (2004), New perspectives on Titan's upper atmosphere from a reanalysis of the Voyager 1 UVS solar occultations, *Icarus*, *170*, 91–112, doi:10.1016/j.icarus.2004.03.005.
- Waite, J. H., et al. (2004), The Cassini Ion and Neutral Mass Spectrometer (INMS) investigation, *Space Sci. Rev.*, *114*, 113–231, doi:10.1007/s11214-004-1408-2.
- Wilson, E. H., and S. K. Atreya (2004), Current state of modeling the photochemistry of Titan's mutually dependent atmosphere and ionosphere, *J. Geophys. Res.*, *109*, E06002, doi:10.1029/2003JE002181.
- Yelle, R. V., J. Cui, and I. C. F. Müller-Wodarg (2008), Methane escape from Titan's atmosphere, *J. Geophys. Res.*, *113*, E10003, doi:10.1029/2007JE003031.
- Yung, Y. L., M. Allen, and J. P. Pinto (1984), Photochemistry of the atmosphere of Titan: Comparison between model and observations, *Astrophys. J. Suppl. Ser.*, *55*, 465–506, doi:10.1086/190963.
- A. Bar-Nun, Department of Geophysics and Planetary Sciences, Tel Aviv University, Tel Aviv 69978, Israel.
- J. M. Bell, A. D. DeJong, V. De La Haye, G. Fletcher, D. Gell, B. A. Magee, K. E. Mandt, and J. H. Waite Jr., Division of Space Science and Engineering, Southwest Research Institute, 6220 Culebra Rd., PO Box 28510, San Antonio, TX 78228, USA. (jbell@swri.edu)
- S. W. Bougher, A. J. Ridley, and G. Toth, Department of Atmospheric, Oceanic, and Space Sciences, University of Michigan, Ann Arbor, MI 48109, USA.
- R. Jacovi, Ice Spectroscopy Laboratory, Jet Propulsion Laboratory, California Institute of Technology, Pasadena, CA 91109, USA.
- J. Westlake, Department of Physics and Astronomy, University of Texas at San Antonio, San Antonio, TX 78249, USA.